

The 5-THz metal-mesh filters based on Mylar film

Qiang Zhi(支强), Jiameng Wang(王家萌), Wei Geng(耿伟), Yuhao Hu(胡雨浩), Hao Wu(吴昊), Kangmin Zhou(周康敏), Jiangqiao Ding(丁江乔), Jie Hu(胡洁), Zheng Wang(王争), Wei Miao(缪巍), Jing Li(李婧), and Shengcai Shi(史生才)

Citation: Chin. Phys. B, 2025, 34 (**11**): 118401. DOI: 10.1088/1674-1056/addbca
http://cpb.iphy.ac.cn; http://iopscience.iop.org/cpb

What follows is a list of articles you may be interested in

Switchable and tunable triple-channel bandpass filter

Ming-En Tian(田明恩), Zhi-He Long(龙之河), Li-Jun Feng(冯丽君), Lei-Lei He(贺磊磊), and Tian-Liang Zhang(张天良)

Chin. Phys. B, 2022, 31 (**7**): 078401. DOI: 10.1088/1674-1056/ac4f4f

Theoretical and experimental study on frequency pushing effect of magnetron

Kang Li(李慷), Yi Zhang(张益), Hua-Cheng Zhu(朱铧丞), Ka-Ma Huang(黄卡玛), Yang Yang(杨阳)

Chin. Phys. B, 2019, 28 (**11**): 118402. DOI: 10.1088/1674-1056/ab4d3d

Modeling and experimental studies of a side band power re-injection locked magnetron

Wen-Jun Ye(叶文军), Yi Zhang(张益), Ping Yuan(袁萍), Hua-Cheng Zhu(朱铧丞), Ka-Ma Huang(黄卡玛), Yang Yang(杨阳)

Chin. Phys. B, 2016, 25 (**12**): 128402. DOI: 10.1088/1674-1056/25/12/128402

Improving the performance of perovskite solar cells with glycerol-doped PEDOT:PSS buffer layer

Jian-Feng Li(李建丰), Chuang Zhao(赵创), Heng Zhang(张恒), Jun-Feng Tong(同军锋), Peng Zhang(张鹏), Chun-Yan Yang(杨春燕), Yang-Jun Xia(夏养君), Duo-Wang Fan(范多旺)

Chin. Phys. B, 2016, 25 (**2**): 028402. DOI: 10.1088/1674-1056/25/2/028402

Cubature Kalman filters： Derivation and extension

Zhang Xin-Chun (张鑫春), Guo Cheng-Jun (郭承军)

Chin. Phys. B, 2013, 22 (**12**): 128401. DOI: 10.1088/1674-1056/22/12/128401

The 5-THz metal-mesh filters based on Mylar film

Qiang Zhi(支强)[1,2], Jiameng Wang(王家萌)[1,2], Wei Geng(耿伟)[1,2], Yuhao Hu(胡雨浩)[1,2], Hao Wu(吴昊)[1,2], Kangmin Zhou(周康敏)[1], Jiangqiao Ding(丁江乔)[1], Jie Hu(胡洁)[1], Zheng Wang(王争)[1], Wei Miao(缪巍)[1], Jing Li(李婧)[1], and Shengcai Shi(史生才)[1,†]

[1] *Purple Mountain Observatory, Chinese Academy of Sciences, Nanjing* 210023, *China*
[2] *School of Astronomy and Space Sciences, University of Science and Technology of China, Hefei* 230026, *China*

(Received 12 March 2025; revised manuscript received 18 April 2025; accepted manuscript online 22 May 2025)

Imaging detector arrays have been widely used in terahertz (THz) astronomical observations, where optical filters play an important role. In this work, a 5-THz metal-mesh bandpass filter (MMBF) using cross-slot-shaped resonators is developed and fabricated on Mylar film through photolithography. Extensive simulations, accounting for factors such as Mylar film loss, surface conductivity, corner errors, and surface roughness, were conducted to assess their impact on the filter's performance. The measured characteristics, including a center frequency of 5.06 THz, a transmittance of 62%, and a 3-dB fractional bandwidth (FBW) is 38%, obtained via Fourier-transform infrared spectroscopy (FTIR), closely match the simulation results. This scalable metal-mesh filter shows promise for future THz astronomical applications.

Keywords: metal-mesh filter, Mylar film, transmittance

PACS: 84.30.Vn, 85.25.Pb, 87.50.U–, 07.57.–c

DOI: 10.1088/1674-1056/addbca **CSTR:** 32038.14.CPB.addbca

1. Introduction

Terahertz (THz) astronomical observations play a pivotal role in characterizing interstellar dust and unraveling galaxy evolution.[1–3] Pioneering instruments, such as Herschel/PACS, IRAS, and AKARI/FIS, have advanced far-infrared spectroscopy using Ge: Ga photoconductors and silicon bolometers at 60 μm.[1–3] Recent advancements in superconducting detectors, including kinetic inductance detectors (KIDs) and transition edge sensor (TES), have garnered significant attention due to their ultralow noise ($<10^{-18}$ W/Hz$^{0.5}$)[4] and wide frequency detection range in the THz band.[5,6]

In these imaging detector arrays, filters along the optical path play a critical role in defining the detection band. Highly integrated on-chip filters have been widely used in spectrometers such as DESHIMA[7] and SuperSpec,[8] but their operational range is typically limited to below 350 GHz. In contrast, metal-mesh filters fabricated from patterned Cu or Au sheets dominate THz filtering applications, existing in two primary forms: freestanding electroplated grids[15–18] and substrate-supported form.[9–14] Commercial filters, such as those from QMC, TYDEX and Thorlabs, are also available. There are many other methods that can improve filter designs, but they are not applicable to this 5-THz filter design, and achieving high transmittance remains a challenge.[19–22]

Table 1 has listed the results from different groups worldwide for substrate-supported filters. These studies have explored different substrates and successfully expanded the frequency from 0.5 THz to 7.9 THz, serving as a reference for the work in this article. While freestanding filters offer superior passband transmission through minimized dielectric losses, substrate-supported filters provide distinct advantages for cryogenic detectors. These filters are easier to fabricate and exhibit greater stability. Moreover, the dielectric loss of the substrates can be reduced when they are cooled to cryogenic temperatures.[10] In THz applications, the choice of substrate material is critical for minimizing signal loss. As demonstrated in Table 1, the filter designed in this work achieves higher operational frequencies and improved transmittance compared to those fabricated on high-density polyethylene (HDPE) substrates. Among available material options, Mylar is particularly well-suited for this purpose due to several advantageous properties: high transmittance ($>77\%$) for frequencies above 1 THz, superior mechanical and thermal stability at low temperatures compared to materials like HDPE,[11] and enhanced adhesion to metallic layers, which is essential for reliable device fabrication.

In this work, a cross-slot-shaped metal-mesh filter based on Mylar film was designed for a 5-THz KIDs array.[23] Electrically thin Mylar films were selected, and various thicknesses were tested to optimize transmittance in a range of 3 THz–7 THz. The filters were fabricated in a cleanroom using photolithography. A transmittance of 62% with a 3-dB fractional bandwidth (FBW) of 38% at 5.06 THz was obtained using a Fourier transform infrared (FTIR) spectrometer. Through systematic analysis, excellent agreement was achieved between the simulated and experimental performance, validating both the design methodology and the fabrication approach.

†Corresponding author. E-mail: scshi@pmo.ac.cn

© 2025 Chinese Physical Society and IOP Publishing Ltd. All rights, including for text and data mining, AI training, and similar technologies, are reserved.

Table 1. Measurement results of metal-mesh bandpass filters from different groups.

Groups	Frequency (THz)	Transmission (%)	3-dB FBW (%)	Substrate/fabrication process
Ref. [9]	0.51	78	33	Mylar/photolithography
Ref. [10]	2.20	64	28	Mylar/photolithography
Ref. [11]	2.91	52	14	HDPE/photolithography
Ref. [13]	7.90	52	15	polyimide/photolithography
This work	5.06	62	38	Mylar/photolithography

2. Filter design and fabrication

A metal-mesh filter at 5 THz using a cross-slot array is proposed in this work. As is well known, the filter structure becomes smaller in the THz regime. Compared with the traditional split-ring shape, the resonant frequency of the cross-slot shape is less sensitive to the size tolerance and is thus easy to fabricate. Compared with the H and split-ring shape, the cross-slot shape has rotational symmetry and does not require polarization alignment. The filter characteristics are predominantly governed by three geometric parameters: period (P), cross-length (L), and cross-width (W), as detailed in Ref. [10]. A systematic parametric analysis was performed through numerical simulations to evaluate the influence of three geometric parameters on both central frequency and transmission efficiency. As illustrated in Fig. 1, among the three parameters, the length exhibits the most significant influence on the center frequency, while the period and width demonstrate more substantial impacts on both transmittance and bandwidth characteristics. These simulations are consistent with the results in the references.[9–11]

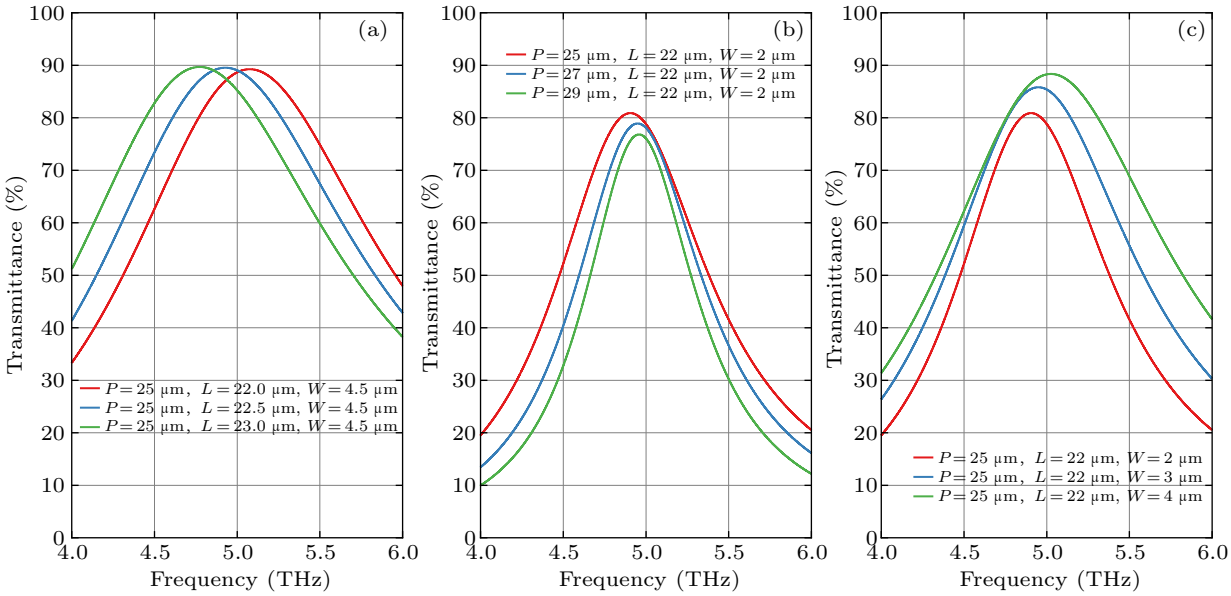


Fig. 1. Varied filter characteristics with length (a), period (b), and width (c).

The center frequency is also influenced by the dielectric properties of the Mylar substrate. The refractive index ($n \approx 1.7$) and absorption coefficient ($\alpha \approx 50$ cm^{-1}) of Mylar at 5 THz were obtained from the literature,[24] yielding a calculated relative permittivity ($\varepsilon_r \approx 2.89$) and loss tangent ($\tan\delta \approx 0.028$) at this frequency. In the HFSS simulations, periodic boundary conditions were implemented to efficiently approximate the infinite grid behavior through a single-unit cell analysis, significantly reducing computational complexity. Figure 2(a) illustrates the designed square unit cell. Cross-slot shape with optimized geometric parameters ($P = 25$ μm, $L = 21.5$ μm, and $W = 3.5$ μm) were patterned on a golden film based on Mylar substrate. The ideal conductivity of Au used in the simulation is 4.1×10^7 S/m. The HFSS model, as shown in the inset of Fig. 2(b). The simulation result is shown in Fig. 2(b). An 80% transmittance and a 40% 3-dB FBW were achieved at the center frequency of 4.96 THz.

The skin depth (δ) of gold at 5 THz was calculated to be 35 nm using the classical formula $\delta = \sqrt{2/\omega\mu\sigma}$. To ensure adequate electromagnetic confinement, the gold film thickness was designed to far exceed the skin depth, with a thickness of 300 nm chosen. The simulation results in Fig. 3(a) illustrates that a reduction in surface conductivity leads to a pronounced decrease in transmittance. This observation highlights the dominant role of surface conductivity in governing the electromagnetic response of conductive layers at THz frequencies,

particularly in modulating transmittance performance. The experiment in MacDonald's article[10] shows a similar conclusion. The smaller the DC surface resistance, the larger the transmittance of the filter will be. When the film thickness is much greater than the skin depth (δ), the surface impedance can be expressed as $Z_S = (1+j)/(\delta\sigma)$, which is a function of temperature.

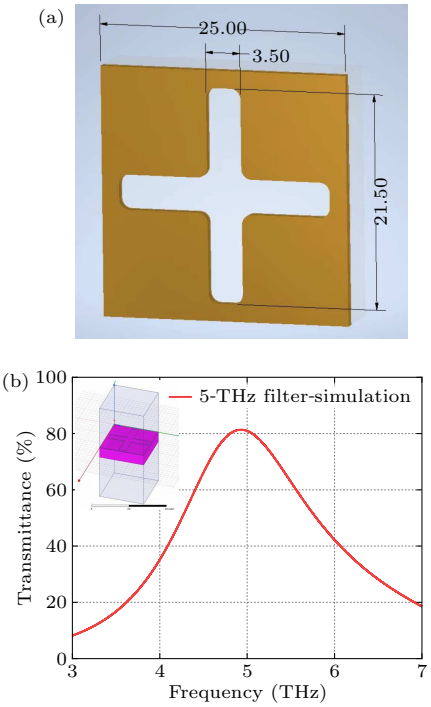


Fig. 2. (a) Filter geometry and the square unit cell, golden film with cross-slot-shape based on Mylar film. (b) Simulation filter characteristics. The inset is the simulation model in HFSS.

Additionally, fabrication-induced geometric imperfections at the edges of the cross-shaped apertures were analyzed. Figure 3(b) illustrates the corner error (fillet radius (r)/cross-width (W), which is a critical manufacturing tolerance parameter. Simulations reveal that such corner errors not only induce shifts in center frequency but also degrade peak transmittance, highlighting the importance of precise process control in device realization.

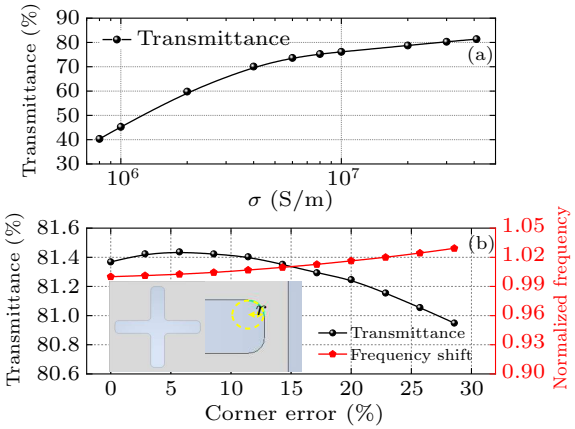


Fig. 3. The effect of (a) surface conductivity and (b) corner error on the transmittance of the filter.

These filters were fabricated on 3.5/6.0-μm-thick Mylar films using a standard lithography process. First of all, the Mylar substrate needs to be fixed on the silicon wafer with a flat surface. A 2-inch (1 inch = 2.54 cm) silicon wafer was spin-coated with photoresist AZ 1500 rpm at 3000 rpm for 30 s to achieve uniform adhesion. To ensure the flatness of the Mylar film, the film was sandwiched between two Si wafers in Fig. 4(a). And then thermally cured at 95 °C for 120 s. This critical step eliminated wrinkles and ensured uniform contact between the Mylar and the silicon wafer, minimizing focusing issues during exposure.[10] After substrate stabilization, as shown in Fig. 4(b) the second step is to cut the excess Mylar and apply uniform glue on the surface of Mylar. Photoresist AZ 5214E was spin-coated at 4000 rpm (∼ 1.2-μm thickness) and soft-baked at 100 °C for 90 s on a precision hotplate. Then the sample underwent pattern exposure, followed by uniform flood exposure to the entire substrate after a post-exposure bake at 110 °C for 120 s. After that, a development in AZ 300 MIF for 45 s revealed a high-quality cross-shaped pattern. These two steps correspond to exposure and development in Figs. 4(c) and 4(d). The last step is deposition and lift off. A 300-nm thick gold layer was deposited at a current of 0.3 A and a pressure of 9-mTorr (1 Torr = 1.33322×10^2 Pa) argon, with the substrate temperature maintained below 50 °C to prevent thermal deformation of the Mylar, as given in Fig. 4(e). The lift-off process was performed by immersing the sample in acetone for 12 hours, followed by rinsing with alcohol. Meanwhile, the Mylar film will be removed from the silicon wafer.

After the lithography process, the filter was mounted on custom aluminum rings to ensure mechanical stability, as shown in Fig. 4(h). The structural details of the cross-shaped slot is presented in Fig. 4(i).

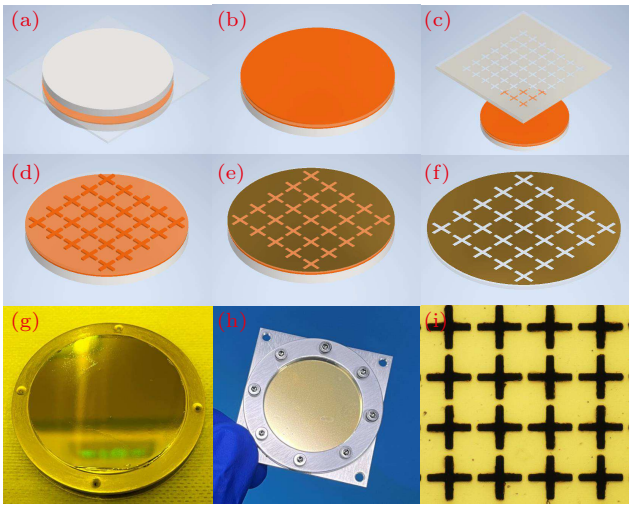


Fig. 4. (a) Mylar film was sandwiched between two Si wafers, (b) Mylar film was cut and spin-coated with photoresist, (c) exposure, (d) developed, (e) deposit gold film and lift off, (f) remove Mylar film from the silicon wafer, (g) Mylar film after gold sputtering, (h) final filter mounted on an aluminum ring, and (i) cross-slot structures under an optical microscope.

3. Characterization and result analysis

3.1. Mylar substrate testing at 5 THz

Considering the high-frequency loss and changes in the dielectric constant of the Mylar substrate, two different thicknesses of Mylar substrates (3.5 μm and 6 μm) were tested using a Fourier transform infrared (FTIR) spectrometer. As shown in Fig. 5, the measured transmittance at 5 THz for the 3.5-μm-thick and 6-μm-thick Mylar were 85.6% and 77.8%, respectively.

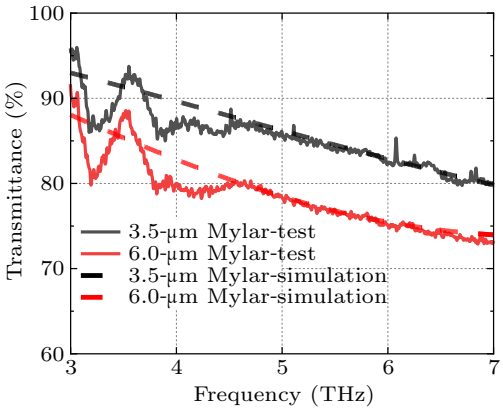


Fig. 5. Experimental and simulation results for Mylar substrates of different thicknesses.

Finite element analysis of the Mylar dielectric properties revealed consistent relative permittivity values of approximately 2.89 at 5 THz for both thicknesses. However, different loss tangents were observed: 0.055 for the 3.5-μm substrate and 0.025 for the 6-μm substrate. This discrepancy may be due to variations between different product batches. Subsequent filter simulation analyses were conducted based on these experimental results.

3.2. Performance analysis

This 5-THz filter has been measured using the same FTS system. A transmittance of 62% at the center frequency of 5.06 THz and a 3-dB FBW of 38% have been obtained, as shown in Fig. 6. There are slightly different results compared with the simulation results in Fig. 2, mainly for two reasons as fabrication tolerance and conductivity effect. The geometric parameters of the cross-slot were measured, including the period (24.96 μm), length (21.3 μm), width (3.4 μm) and the gold film thickness (330 nm). To obtain an accurate conductivity, a 300-nm-thick Au film deposited on a Mylar substrate was characterized using the four-point probe method. The measured surface conductivity is 2×10^7 S/m, only half of the ideal one.

Considering the influence of metal surface roughness on surface electrical conductivity, the atomic force microscopy (AFM) and laser confocal microscopy were employed to quantify surface roughness over a representative 25 μm×25 μm unit area. As shown in Fig. 7, the root-mean-square roughness (S_q) measured 10 nm for the planar Au film region, while the patterned region exhibited significantly higher roughness ($S_q = 166$ nm). As illustrated in Fig. 7(b), the primary contributor to this increased roughness was irregular edge fluctuations along the patterned structures. Developed to calculate the correction factor for predicting the conductivity of rough metal, an experimental formula based on the Groiss model[25] was used to achieve an equivalent conductivity of approximately 4×10^6 S/m.

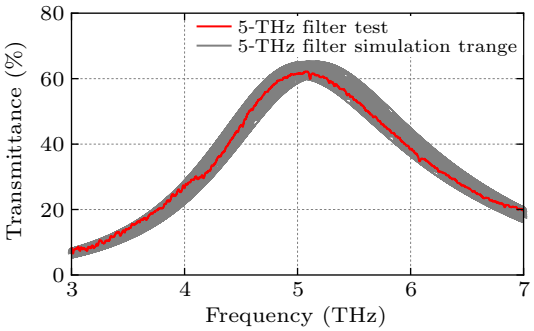


Fig. 6. Experimental transmittance along with multiple simulation data.

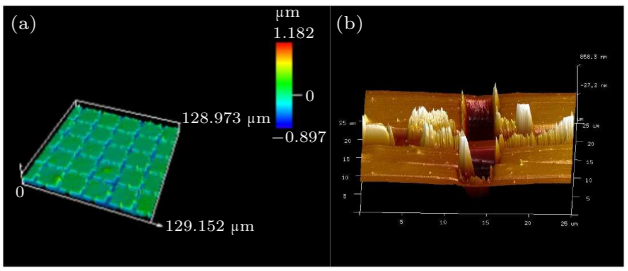


Fig. 7. (a) Surface roughness measurement by laser confocal microscopy within 129 μm×129 μm, (b) the 3D structure obtained by AFM within a representative 25 μm×25 μm unit area.

Based on the above discussion, the measured geometric parameters and equivalent conductivity can be incorporated into the HFSS model and re-simulated. In addition, a series of scanning parameter results including corner error ($r/W = 0\%$–30%) and surface conductivity ($\sigma \approx 2\times10^6$ S/m) were simulated and given in Fig. 6 (gray lines). As can be seen, the measured results are highly consistent with the re-simulation results and are within the error range.

To further enhance the filter performance, several improvements can be made. Firstly, the surface flatness and conductivity of the gold layer can be improved. Secondly, a substrate with a higher transmission rate at 5 THz, such as a thinner Mylar film, can be chosen. Additionally, new structural designs, such as multi-layer structures, can also be attempted.

4. Conclusion

In conclusion, a Mylar-based 5-THz metal-mesh bandpass filter with cross-slot-shaped resonators was successfully

designed, fabricated, and characterized. The filter demonstrated a peak power transmission of 62% at 5.06 THz and a 3-dB FBW of 38%. The effects of Mylar film loss, surface conductivity, corner errors, and surface roughness were thoroughly analyzed. Experimental results showed good agreement with the simulations. This work provides a valuable reference for designing filters in the high-frequency THz range and supports the future application of low-temperature superconducting detectors in the THz frequency band.

Acknowledgements

Project supported in part by the National Key Research and Development Program of China (Grant No. 2023YFA1608200), the National Natural Science Foundation of China (Grant No. 12020101002), and the Fund from the Chinese Academy of Sciences (Grant No. PTYQ2024BJ0010). The FTIR measurements were supported by the Shanghai Institute of Microsystem and Information Technology.

References

[1] Poglitsch A, Waelkens C, Geis N, *et al*. 2010 *Astron. Astrophys*. **518** L2

[2] Sanders D B, Mazzarella J M, Kim D C, Surace J A and Soifer B T 2003 *Astron. J.* **126** 1607

[3] Takita S, Doi Y, Ootsubo T, *et al*. 2015 *Publ. Astron. Soc. Jpn.* **67** 51

[4] Shi Q, Li J, Zhi Q, Wang Z, Miao W and Shi S C 2022 *Sci. China-Phys. Mech. Astron.* **65** 239511

[5] Shi S C, Paine S, Yao Q J, Lin Z H, Li X X, Duan W Y, Matsuo H, Zhang Q Z, Yang J, Ashley M C B, Shang Z H and Hu Z W 2016 *Nat. Astron.* **1** 0001

[6] Li J, Deng X J, Li Y, Hu J, Miao W, Lin C X, Jiang J and Shi S C 2025 *Research* **8** 0586

[7] Redford J, Wheeler J, Karkare K, Hailey-Dunsheath S, Bradford C M, Shirokoff E, Barry P S, Che G, Glenn J, Leduc H G, Mauskopf P, McGeehan R, Reck T and Zmuidzinas J 2018 *Millimeter, Submillimeter and Far-Infrared Detectors and Instrumentation for Astronomy IX. SPIE*, June 10–15, 2018, Austin, Texas, USA, p. 354

[8] Endo A, Karatsu K, Laguna A P, *et al*. 2019 *J. Astron. Telesc. Instrum. Syst.* **5** 035004

[9] Page L, Cheng E S, Golubovie B, Gundersen J and Meyer S S 1994 *Appl. Opt.* **33** 11

[10] MacDonald M E, Alexanian A, York R A, Popovic Z and Grossman E N 2000 *IEEE Trans. Microw. Theory Tech.* **48** 712

[11] Ma Y, Khalid A, Drysdale T D and Cumming D R 2009 *Opt. Lett.* **34** 1555

[12] Kuznetsov S A, Kubarev V V, Kalinin P V, Goldenberg B G, Eliseev V V, Petrova E V and Vinokurov N A 2007 29*th International Free Electron Laser Conference, FEL,* August 26–32, 2007, Novosibirsk, Russia, p. 89

[13] Smith H A, Rebbert M and Sternberg O 2003 *Appl. Phys. Lett.* **82** 3605

[14] Chen Y, Huang F, Liang B, Su H, Ju X and Wang X A 2025 *IEEE Trans. THz Sci. Technol.* 1

[15] Porterfield D W, Hesler J L, Densing R, Mueller E R, Crowe T W and Weikle R M 1994 *Appl. Opt.* **33** 6046

[16] Yoo C, Hesler J L and Karasik B S 2025 *IEEE Trans. THz Sci. Technol.* **15** 296

[17] Möller K D, Warren J B, Heaney J B and Kotecki C 1996 *Appl. Opt.* **35** 6210

[18] Melo A M, Gobbi A L, Piazzetta M H and Da Silva A M 2012 *Adv. Opt. Technol.* **2012** 530512

[19] Zhang Y J, Li C L, Luan J Q, Zhao M, Gao D S and Li P L 2024 *Chin. Phys. B* **33** 104210

[20] Li J W, Zhang W, Liu X F and Yao X R 2024 *Chin. Phys. B* **33** 114201

[21] Karahan E A, Liu Z, Gupta A, Shao Z, Zhou J, Khankhoje U and Sengupta K 2024 *Nat. Commun.* **15** 10734

[22] Wang Y, Qi F, Zhang Z X and Wang J K 2023 *Chin. Phys. B* **32** 038702

[23] Zhi Q, Geng W, Lv W T, Lin Z H, Zhou K M, Li J and Shi S C 2023 *Infrared, Millimeter-Wave and Terahertz Technologies X. SPIE,* October 14–17, 2023, Beijing, China, p. 28

[24] Loewenstein E V and Smith D R 1971 *Appl. Opt.* **10** 577

[25] Groiss S 1996 *Numerical Analysis of Lossy Cavity Resonator* Ph.D. Dissertation (Graz: Technical University of Graz) (in German)